Quantum cascade lasers operating from 1.4 to 4 THz

(Invited Paper)

Sushil Kumar

Department of Electrical and Computer Engineering and Center for Optical Technologies, Lehigh University, Bethlehem, PA 18015, USA

Corresponding author: sushil@lehigh.edu

Received July 17, 2011; accepted August 18, 2011; posted online September 30, 2011

The development of teranertz (THz) quantum cascade lasers (QCLs) has progressed considerably since their advent almost a decade ago. THz QCLs operating in a frequency range from 1.4 to 4 THz with electron-phonon scattering mediated depopulation schemes are described. Several different types of GaAs/AlGaAs superlattice designs are reviewed. Some of the best temperature performances are obtained by the so-called resonant-phonon designs that are described. Operation above a temperature of 160 K has been obtained across the spectrum for THz QCLs operating at $\nu >$ 1.8 THz. The maximum operating temperature of previously reported THz QCLs has empirically been limited to a value of $\sim \hbar\omega/k_{\rm B}$. A new design scheme for THz QCLs with scattering-assisted injection is shown to surpass this empirical temperature barrier, and is promising to improve the maximum operating temperatures of THz QCLs even further.

OCIS codes: 140.5965, 140.3070.

doi: 10.3788/COL201109.110003.

1. Introduction

High-power sources of terahertz (THz) radiation are required for a multitude of applications in sensing, imaging, and spectroscopy in fields as diverse as astronomy, medicine, security, pharmaceuticals and so-forth. THz science and technology has advanced significantly in the recent years[1,2] especially toward the realization of novel THz radiation sources. In comparison to narrow-band sources such as lasers, broadband sources of terahertz radiation are more widely available; however, such sources are inherently low power (average power is of the order of few micro-Watts). They are useful nevertheless because of room temperature operation and for their ability to be detected coherently. Techniques such as generation of THz bandwidth time-domain pulses in high resistivity semiconductors[3], non-linear generation by electro-optical-rectification in crystals such as ZnTe[4], or non-linear generation by optical parametric conversion in materials such as $LiNbO_3$[5] or by difference-frequency generation in semiconductors[6], have been used for various raster-scanned imaging and broadband spectroscopic applications.

However, there has been a dearth of compact solid-state terahertz sources that could provide large (>1 mW) amount of average optical power. Additionally, some applications such as heterodyne spectroscopy for molecular sensing inherently require high frequency stability and extremely narrow linewidths which are only available from narrow-band sources such as lasers operating in continuous-wave (CW) mode. From the various available methods of generating coherent terahertz radiation, terahertz quantum cascade lasers (QCLs), which were developed about a decade ago[7], are the most promising among solid-state technologies. THz QCLs are semiconductor lasers in which radiation is due to electronic intersubband transitions in semiconductor superlattices that have been demonstrated in GaAs/AlGaAs[7], InGaAs/InAlAs[8], and InGaAs/GaAsSb[9] heterostructures. These devices now provide CW spectral coverage in the frequency range of 1.2 THz ($\lambda \sim 250$ μm) through $\nu \sim 5$ THz ($\lambda \sim 60$ μm) with optical power output in the tens of milliWatt range[10,11]. In terms of optical power output, frequency linewidth, and frequency stability they are arguably at par with the much bigger and expensive molecular gas lasers. Additionally their emission frequency could be artificially adjusted by bandstructure engineering, which makes them attractive for a variety of applications. However, cryogenic cooling is required for their operation which is the primary hindrance towards making a THz QCL available in a compact and inexpensive instrument.

With recent demonstrations of real-time imaging[12] and heterodyne spectroscopy[13] using THz QCLs, they have come a long way in meeting some of important characteristics required from such narrowband THz sources for the targeted applications in spectroscopy, imaging, and remote-sensing. However, the requirement for cryogenic cooling is an impediment toward their practicability and cost-effectiveness, and therefore, improvement of their operating temperatures is one of the most important research goals in the field. The best performing THz QCLs in terms of operating temperature employ the fast scattering of electrons due to longitudinal-optical (LO) phonons in the polar III-V semiconductor materials as a means to establish population inversion for optical gain. Operation above 160 K has now been demonstrated in frequencies ranging from 1.8[14] to 4.4 THz[15] from such designs. The highest maximum operating temperature of 186 K for THz QCLs is obtained for a 3.9 THz design with a diagonal radiative transition[16]. This paper summarizes a variety of THz QCLs across the frequency range from 1.4 to 4 THz with electron-LO-phonon scattering assisted depopulation schemes. The recent development of a THz QCL with scattering-assisted injection[14] is shown

to be promising way forward to further improve the temperature performance of THz QCLs.

2. Resonant-phonon depopulation scheme

As opposed to the chirped superlattice[7] and the bound-to-continuum[19] design schemes, the first THz QCL based on a electron-phonon scattering assisted depopulation introduced a "resonant-phonon" depopulation scheme[18], which has now become the basis for some of the best performing THz QCL designs. The original THz QCL design with such a depopulation scheme is shown in Fig. 1(b). The key feature of that design is in its unique depopulation mechanism, which occurs by a combination of the resonant tunneling of the electrons from the active region wells on the left to the injector region wells on right, and a fast electron-phonon scattering process within the injector wells. The resonant-tunneling is due to the strongly anticrossed doublet of lower radiative subbands 3 and 4, which leads to selective transport of the electrons in the lower radiative subband to the wide injector wells. The tunneled electrons then emit LO-phonons on a sub-ps time-scale owing to the resonant energy separation of the equivalent of a LO-phonon between the excited and the ground states in the injector region.

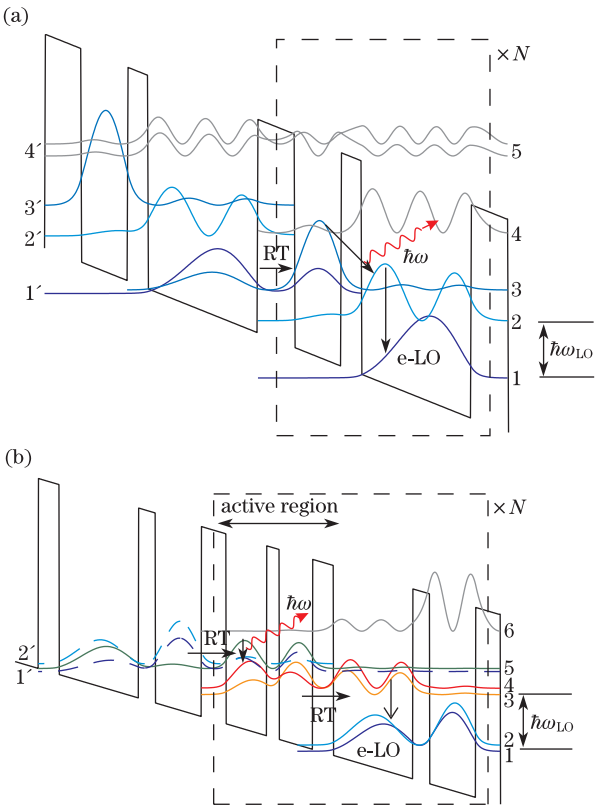

Fig. 1. (a) Operating bias conduction band diagram showing two modules of one of the simplest possible THz QCL design with three-subbands and two-wells per module[17]. Moduli-squared wavefunctions are vertically displaced in the GaAs/$Al_{0.15}Ga_{0.85}As$ superlattice according to their energies. Subbands 3 and 2 are the radiative subbands and subband 1 is the injector subband; (b) conduction band diagram for a five-subband THz QCL design with the "resonant-phonon" depopulation scheme[18]. The radiative transition is between subbands 5 and 4, subbands 3 and 4 are strongly anticrossed at the operating bias, and the anticrossed doublet of subbands 1 and 2 are the injector subbands.

Several other THz QCL designs schemes with phonon-assisted depopulation have been reported[17,20,21]. The simplest of those is a "direct-phonon" depopulation scheme for a two-well THz QCL design as shown in Fig. 1(a). However, in terms of maximum temperature of operation T_{max} that determines the robustness of the population inversion against an increase in lattice temperature, resonant-phonon designs have performed consistently better. For example, T_{max}=169 K for a variant of the original resonant-phonon design with five-subbands as shown in Fig. 1(b)[22] whereas the two-well design of Fig. 1(a) led to a best $T_{max} \sim 125$ K[23].

The primary feature of the resonant-phonon depopulation mechanism is the spatial isolation of the upper radiative subband from the wider wells in the injector region, which is made possible owing to the selective and bias-dependent resonant-tunneling process for extracting electrons out of the lower radiative subband. Such a design scheme makes the upper-subband lifetime due to electron-LO-phonon scattering longer owing to the reduced overlap between the upper radiative subband and the injector subbands. Additionally, even at higher temperatures, the likeliness of phonon re-absorption from the upper subband to the the excited states in the injector region is reduced, which weakens an important leakage path for the electrons as the lattice temperature increases[17].

3. THz QCLs with one-well injectors

Initial demonstrations of different types of THz QCLs had a common attribute in that all the designs had multiple injector wells and therefore multiple injector subbands[7,18,19,24]. Multiple injector wells were thought necessary to minimize parasitic current flow at low bias and to optimize current transport across the quantum structure close to the operating bias. However, designs with multiple injector subbands introduce extra optical losses in the gain medium owing to intersubband absorption of radiation, especially when the energy separation between the subbands within the injector region is close to the radiative frequency of the QCL structure. Additionally, electron population gets spread in energy space with multiple injector subbands, which decreases the injection selectivity of electrons from injector region to the adjacent module's upper radiative subband by the mechanism of resonant-tunneling. A one-well injector design was initially demonstrated to achieve operation of a THz QCL below 2 THz[25] owing to its superior injection selectivity, which becomes a critical requirement for low-frequency THz QCLs. An added advantage of such a design scheme is that it affords a greater design flexibility in the design of the active region. In this section, we discuss several THz QCLs with one-well injector regions operating across different frequencies in the terahertz spectrum. For frequencies above 2 THz, the highest operating temperatures for THz QCLs are all obtained by designs with such an injection scheme.

A. Diagonal radiative transition with two-well active region

The original one-well injector design consisted of three-wells in the active region (four-wells overall per QCL period) and operated at 1.9 THz[25]. Subsequently, a modified design was published for high frequency operation at 3.4 THz and was further simplified with just three-wells per QCL period[27]. The reduction in number of wells in the active region is advantageous because it offers reduced number of interfaces for a more coherent quantum-transport across the QCL structure. However, the upper radiative subband is less isolated from the injector well in that case, which leads to an increase in carrier leakage from the upper radiative subband to the injector subband and other excited subbands in the injector well. It is likely for this reason that the original three-well QCL design as reported in Ref. [27] had only a moderately good temperature performance with a maximum lasing temperature of 142 K, which was slightly worse than the optimum four-well designs of the type shown in Fig. 1(b) at the time of its demonstration.

For an intersubband radiative transition from subband $u \rightarrow l$ with a full-width at half-maximum (FWHM) linewidth of $\Delta\nu$ centered at a frequency $\nu = (E_u - E_l)/(2\pi\hbar)$, the peak intersubband gain g (per unit length) is expressed as

$$g \propto \frac{\Delta n_{ul} \cdot f_{ul}}{\Delta\nu}, \tag{1}$$

where Δn_{ul} is the three-dimensional (3D) inverted population density, $f_{ul} \propto z_{ul}^2$ is the unitless oscillator strength, $z_{ul} \equiv \langle u|\hat{z}|l\rangle$ is the radiative dipole matrix element with z being the dimension in the growth direction. The performance of the original three-well QCL design from Ref. [27] was improved considerably by significantly lowering the radiative oscillator strength of the design, i.e. by making the design "diagonal"[16]. Such a design has shown the best temperature performance for any THz QCL to-date with a $T_{\max} \sim 186$ K for a 3.9-THz QCL. The design-bias conduction band diagram and experimental results in pulsed operation from a representative device are shown in Fig. 2. A design with a diagonal radiative transition (i.e. a small radiative oscillator strength f_{ul}) keeps τ_{ul} large, especially at higher temperatures when thermally activated LO-phonon scattering from $u \rightarrow l$ tends to diminish the population-inversion[10]. The upper-state lifetime decreases with temperature with an inverse exponential relation

$$\tau_{ul} \propto \exp\left(\hbar\omega_{\mathrm{LO}} - E_{ul}\right)/k_{\mathrm{B}}T_{\mathrm{e}}, \tag{2}$$

where T_{e} is the temperature of the two-dimensional (2D)-electron gas in the upper subband. It was shown in Ref. [16] that the figure-of-merit $f_{ul}\Delta n_{ul}$ improves even as f_{ul} decreases due to diagonality, and hence peak gain remains high even at higher operating temperatures.

An additional and possibly more important advantage of a diagonal design is the fact that it spatially isolates the upper radiative subband from the injector subband, which also increases the upper-subband lifetime as discussed previously. This is particularly necessary for the three-well design shown in Fig. 2(a)

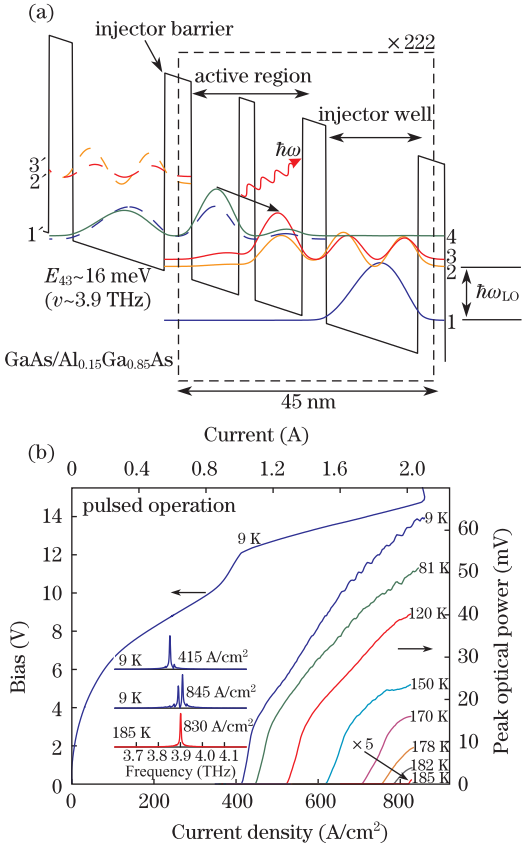

Fig. 2. (a) Operating bias conduction band diagram for a diagonal resonant-phonon design with a one-well injector and two-well active region[16]. The radiative transition is from subband 4 to 3 for which the oscillator strength is $f_{43} \sim 0.38$. The lower radiative subband is depopulated by the resonant-phonon scheme. Starting from the injector barrier, the layer thicknesses in nm are 4.8/8.5/2.8/8.5/4.2/16.4 with the barriers indicated in bold fonts. The widest well is uniformly n-doped to obtain an effective 2D density of 2.17×10^{10} cm^{-2} per period. (b) Experimental characteristics of an edge-emitting metal-metal[26] ridge cavity laser in pulsed operation. The device lased up to a heat-sink temperature of 185 K at a frequency of ~3.9 THz. The best device from this design lased up to a $T_{\max} \sim 186$ K.

since the length of the QCL period for such a design is shorter than QCL designs with more number of wells. Such a spatial isolation of the upper subband also translates into lower parasitic leakage current prior to threshold, which also reduces the threshold current density of the QCL.

B. Vertical radiative transition with three-well active region

A different type of THz QCL with similar functionality to that of the diagonal three-well design discussed in section A is possible without making the radiative transition diagonal. Such a design and the corresponding experimental results are shown in Fig. 3. In this case, the radiative transition is kept vertical, i.e. with a large oscillator strength, however, an additional well is added to the active region[28]. The additional well serves the same purpose as the diagonal radiative transition in that it spatially isolates the upper radiative subband from the wide injector well, thereby

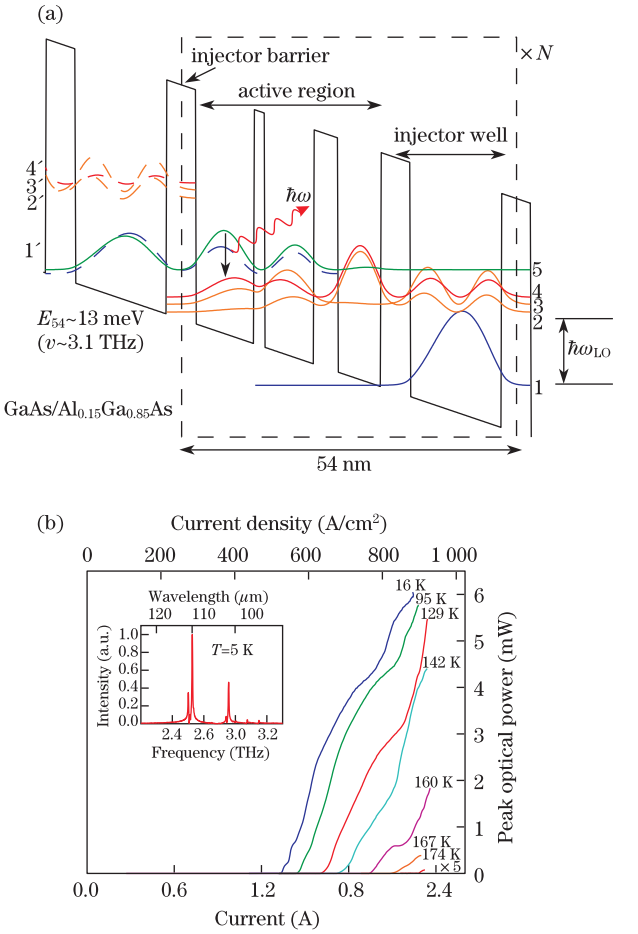

Fig. 3. (a) Operating bias conduction band diagram for a 3 THz QCL design with a three-well active region and one-well injector[28]. The radiative transition is from 5 → 4 for which the oscillator strength is $f_{54} \sim 0.70$. Depopulation of the lower radiative subband is similar to the resonant-phonons scheme of Fig. 1(b), albeit with triplet of strongly anticrossed lower subbands instead of a doublet. Starting from the injector barrier, the layer thicknesses in nm are 4.8/9.4/1.7/8.0/3.9/6.9/4.8/15.8 with the barriers indicated in bold fonts. The widest well is uniformly n-doped to obtain an effective 2D density of 3.0×10^{10} cm^{-2} per period; (b) experimental characteristics of an edge emitting metal-metal ridge laser in pulsed operation. The device lased up to a heat-sink temperature of 174 K at $\nu \sim 3$ THz.

enhancing the upper-subband lifetime. Note that an additional subband appears due to the third-well in the active region, which is then designed to be anticrossed with the lower radiative subband to form a triplet of strongly coupled subbands at the operating bias condition (subbands 2,3,4 in Fig. 3(a)). The maximum operating temperature of 174 K for the 3-THz QCL shown in Fig. 3 is a validation of the advantage of this new design and it is comparable to the best published results for a 3-THz QCL with the three-well active region[31], but with the advantage of significantly lower threshold current densities.

C. Low-frequency design with direct-phonon depopulation

It becomes increasingly difficult to realize QCLs operating below 2 THz. At low frequencies, the laser-level separation E_{ul} (~ 8 meV for $\nu \sim 2$ THz) becomes similar to the typical energy broadening of the subbands (few meVs). Hence, it becomes difficult to selectively inject from $i \rightarrow u$ where i is the injector subband and u is the upper laser subband. For low-frequency QCLs, the injector barrier is typically kept thick to limit the $i \rightarrow l$ leakage-current, which, however, reduces the obtainable dynamic range in current for the laser, and consequently its maximum operating temperature. The lowest frequency for a QCL based on a phonon-depopulation scheme is 1.45 THz ($\hbar\omega \sim 6.0$ meV). The design is similar to the three-subband design in Ref. [17] (Fig. 1(a)), as shown in Fig. 4(a). An additional well is added to the active region to realize larger oscillator strength f_{32} for a fixed injection anticrossing $2\hbar\Omega_{1'3}$ [32,33]. As can be seen from the experimental results from a representative device in Fig. 4(b), the dynamic range in lasing for current is very small, which therefore limits the maximum operating temperature to a relatively small value of 37 K. A

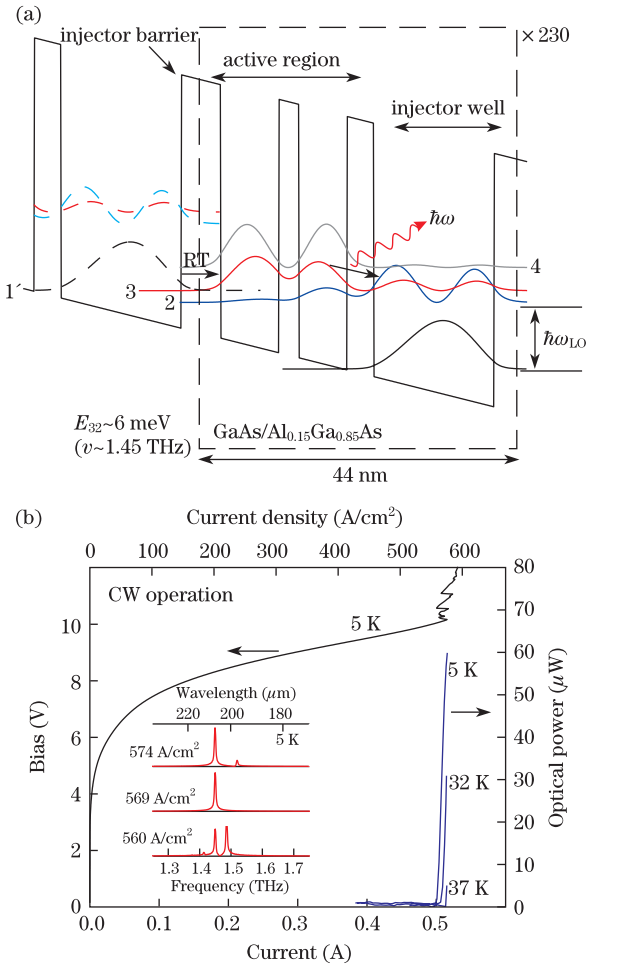

Fig. 4. (a) Operating bias conduction band diagram for a three-well, three-subband 1.45-THz QCL design with direct-phonon depopulation similar to that in Fig. 1(a). The radiative transition is from 3 → 2. Starting from the injector barrier, the layer thicknesses in nm are 5.4/8.2/2.8/6.8/3.8/17.0 with the barriers indicated in bold fonts. The widest well is uniformly n-doped to obtain an effective 2D density of 2.7×10^{10} cm^{-2} per period; (b) experimental characteristics of an edge emitting metal-metal ridge laser in continuous-wave operation. The device lased up to a heat-sink temperature of 37 K at $\nu \sim 1.45$ THz.

better temperature performance for the ν <1.5 THz QCLs is however obtained from a hybrid bound-to-continuum based design scheme[34], where the separation between the lower laser subband and the injector subbands is kept below the LO-phonon energy, which limits the parasitic leakage current density and leads to a greater dynamic range in lasing for current. A 1.2-THz QCL with $T_{\max}$ ~69 K was realized in Ref. [34], which is currently the lowest operating frequency for QCLs without the assistance of an external magnetic field.

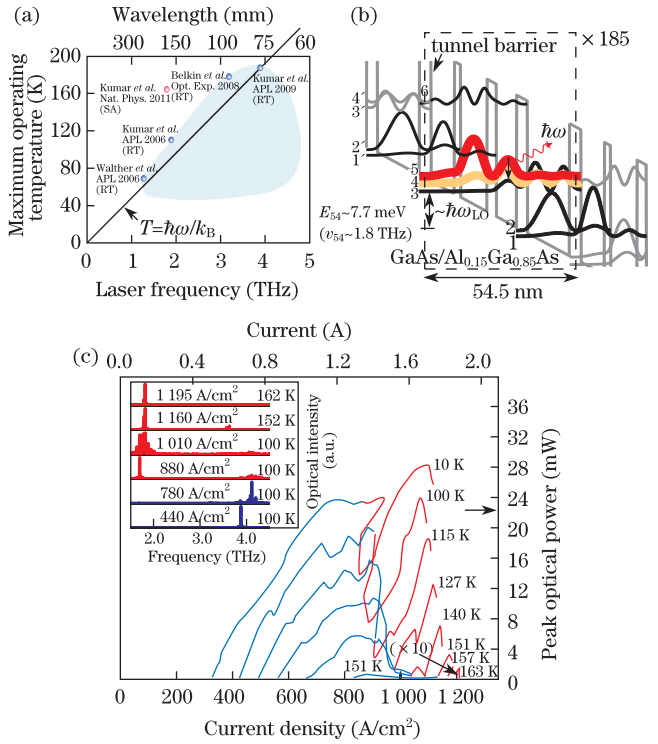

Fig. 5. (a) Survey of maximum operating temperatures for terahertz QCLs with respect to their operating frequency. A variety of designs have been published in literature spread across the shaded region[10]; however, the best performing designs in terms of highest operating temperatures are typically concentrated near the $T_{\max} \sim \hbar\omega/k_{\rm B}$ region. Until recently, all of the previously reported terahertz QCLs relied on a *resonant-tunneling (RT) injection* mechanism; (b) conduction band diagram at operating bias condition for a terahertz QCL with a *scattering-assisted (SA) injection* design scheme[14], where carriers are injected into the upper laser subband by non-radiative scattering (primarily electron-LO-phonon scattering) from the injector subbands. In this case, the radiative transition is from subband $5 \rightarrow 4$ and $1', 2'$ are the injector subbands. Both the depopulation of subband 4 and injection into subband 5 take place via the fast electron-phonon scattering. Starting from the tunnel barrier, the layer thicknesses in nm are 4.2/8.5/2.3/9.6/3.4/7.3/4.0/15.3 with the barriers indicated in bold fonts. The widest well was n-doped to 2.05×10^{16} cm^{-3}; (c) experimental light-current characteristics from the QCL as a function of heat-sink temperature. The device shows dual-color lasing behavior at 4 and 1.8 THz as a function of changing electrical bias. A more robust temperature performance is observed at $\nu \sim 1.8$ THz for which a maximum lasing temperature of $T_{\max} \sim 163$ K $\sim 1.9\hbar\omega/k_{\rm B}$ is observed. This makes it the only solid-state laser operating without magnetic field such that the carrier thermal energy is significantly larger than the photon energy in operation (i.e. $\kappa_{\rm B} T_{\max} > \hbar\omega$). Peak optical power of greater than 2 mW was detected at an operating temperature of 155 K for emission at 1.8 THz.

4. THz QCLs with scattering-assisted injection

A wide variety of THz QCL designs have been reported in Ref. [10]. However, all the previously published THz QCLs rely on a resonant-tunneling (RT) injection scheme to populate the upper laser subband, for which the maximum temperature of operation $T_{\max}$ has been empirically limited to a value $\sim \hbar\omega k_{\rm B}$ across different designs and operating frequencies as shown in Fig. 5(a). This behavior has remained largely inexplicable breeding speculation that a room-temperature THz QCL may not be possible in presently used materials. However, it was recently suggested that such a trend is consequence of the specific resonant-tunneling assisted injection scheme of the previous designs. A new scattering-assisted injection scheme has been developed[14] to surpass this empirical temperature limitation for a 1.8-THz QCL that operates up to $\sim 1.9\ \hbar\omega k_{\rm B}$, which is an unprecedented result for any solid-state laser demonstrated to-date. The design diagram and experimental results from such a device are shown in Figs. 5(b) and (c), respectively. Metal-metal ridge lasers were fabricated and characterized as outlined in Ref. [16]. Pulsed light-current-voltage characteristics and spectra for the QCL are shown in Fig. 5(c). The device lased predominantly at a frequency of 1.8 THz up to a maximum operating temperature of 163 K ($\sim 1.9\ h\nu/k_{\rm B}$). 28 mW of peak optical power was detected at 10 K that reduced to $\sim$ 0.65 mW at 160 K. The results in the power output and operating temperature for this QCL are significantly better than previous THz QCLs operating at similar frequencies[25,35] that are based on the resonant-tunneling injection mechanism, which is likely due to the large gain in this active medium.

Figure 6(a) shows a schematic of the resonant-tunneling injection mechanism that forms the basis for all of the previously reported THz QCLs in literature. In this case, the charge carriers (electrons) are injected into the upper radiative subband u from the injector subband i by the mechanism of resonant-tunneling, which is an efficient process only when the the tunnel barrier is kept thin, or, in other words, the anticrossing splitting energy $2\hbar\Omega_{iu}$ is kept large[32]. However, the laser-level separation E_{ul} for THz frequencies ($E_{ul} \sim 4$ meV for $\nu \sim 1$ THz) is similar to the typical energy broadening of the subbands (a few meVs). Hence, it becomes difficult to selectively inject from $i \rightarrow u$ for a large anticrossing splitting. The injector barrier has therefore to be typically kept thick (RT injected terahertz QCLs with $2\hbar\Omega_{iu} < 2$ meV have shown the best temperature performances). However, in that case, increased operating temperatures degrade the efficiency of the injection process since the injection is now severely effected by the dephasing time T_2^* as shown in Fig. 6(a). In contrast, the scattering-assisted injection scheme of Fig. 6(b) can tolerate much thinner tunnel barriers (i.e. a larger value of anticrossing splitting $2\hbar\Omega_{i_1 i_2}$ in Fig. 6(b)) since the injection into the upper radiative subband u is not via

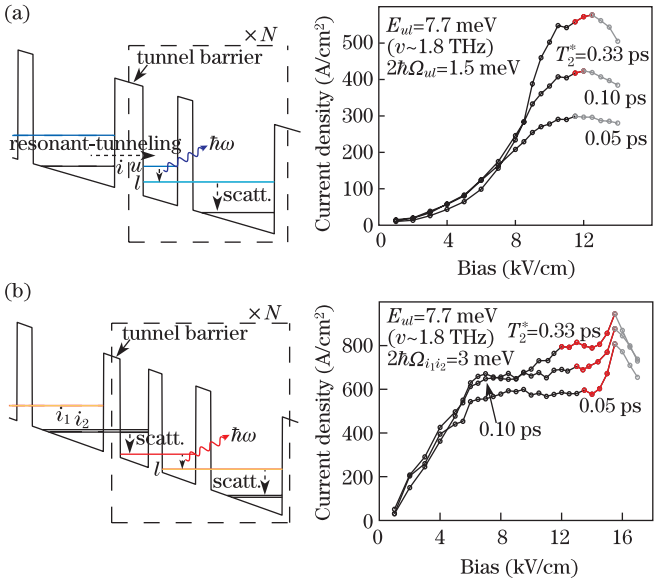

Fig. 6. Effect of reduced dephasing time on THz QCL designs with (a) resonant-tunneling injection and (b) scattering-assisted injection, respectively. Numerical calculations are performed using an ensemble Monte Carlo simulation[29] that accounts for resonant-tunneling transport between neighboring modules of the QCL with a phenomenological dephasing time T_2^*. Higher operating temperatures typically lead to a shorter dephasing times[30]. The computed I-V curves for the QCL designs are highlighted in red color (thick lines) in the bias region with positive population inversion. It can be noted that the design with scattering-assisted injection is more tolerant to a reduced dephasing time T_2^* and achieves population inversion even for a very small T_2^*.

resonant-tunneling, but utilizes electron-phonon scattering (details in Ref. [14]). We have stipulated, as also shown in the calculation in Fig. 6(b), that reduced dephasing times impacts such a design scheme much less severely[14] thereby leading to an improved temperature performance as compared to the designs with resonant-tunneling injection.

The observed threshold current-density Jth for 1.8-THz QCL in Fig. 5(c), remains independent of the heat-sink temperature T approximately up to 110 K, which is a significantly higher turn-on temperature than that for any of the previously reported THz QCLs. The weak temperature dependence of Jth with temperature attests to the robust temperature performance of this design scheme, which is likely due to the fact that the intra-injector anticrossing for this design was $2\hbar\Omega \sim 3$ meV to keep the resonant-tunneling transport across the cascade structure coherent as discussed above. Further improvements in the maximum operating temperature of the design is likely after optimization of the design. This demonstration should be promising for future improvements in the active region of THz QCLs since it shows that variations in the quantum design can significantly alter the device performance.

The work reviewed here was done jointly with Chun W. I. Chan, Qing Hu, and John L. Reno. This work was supported by the National Aeronautics and Space Administration and the National Science Foundation. The work was performed in part at the United States Department of Energy, Center for Integrated Nanotechnologies, and Sandia National Laboratories (Contract DE-AC04-94AL85000).

References

1. B. Ferguson and X.-C. Zhang, Nature Materials **1,** 26 (2006).
2. M. Tonouchi, Nature Photonics **1,** 97 (2007).
3. R. A. Cheville, M. R. Reiten, R. McGowan, and D. R. Grischkowsky, *Sensing with Terahertz Radiation*, D. Mittleman, (eds) (Springer, Berlin, 2003) pp. 237–293.
4. Z. Jiang and X.-C. Zhang, *Sensing with Terahertz Radiation* D. Mittleman, (eds.) (Springer, Berlin, 2003) pp. 155–192.
5. K. Kawase, M. Sato, T. Taniuchi, and H. Ito, Appl. Phys. Lett. **68,** 2483 (1996).
6. W. Shi, Y. Ding, N. Fernelius, and K. Vodopyanov, Opt. Lett. **27,** 1454 (2002).
7. R. Köhler, A. Tredicucci, F. Beltram, H. E. Beere, E. H. Linfield, A. G. Davies, D. A. Ritchie, R. C. Iotti, and F. Rossi, Nature **417,** 156 (2002).
8. L. Ajili, G. Scalari, N. Hoyler, M. Giovannini, and J. Faist, Appl. Phys. Lett. **87,** 141107 (2005).
9. C. Deutsch, A. Benz, H. Detz, P. Klang, M. Nobile, A. M. Andrews, W. Schrenk, T. Kubis, P. Vogl, G. Strasser, and K. Unterrainer, Appl. Phys. Lett. **97,** 261110 (2010).
10. B. S. Williams, Nature Photonics **1,** 517 (2007).
11. G. Scalari, C. Walther, M. Fischer, R. Terazzi, H. Beere, D. Ritchie, and J. Faist, Laser Photonics Rev. **3,** 45 (2009).
12. A. Lee, Q. Qin, S. Kumar, B. S. Williams, Q. Hu, and J. L. Reno, Appl. Phys. Lett. **89,** 141125 (2006).
13. Y. Ren, J. N. Hovenier, R. Higgins, J. R. Gao, T. M. Klapwijk, S. C. Shi, B. Klein, T.-Y. Kao, Q. Hu, and J. L. Reno, Appl. Phys. Lett. **98,** 231109 (2011).
14. S. Kumar, C. W. I. Chan, Q. Hu, and J. L. Reno, Nature Physics **7,** 166 (2011).
15. A. W. M. Lee, Q. Qin, S. Kumar, B. S. Williams, Q. Hu, and J. L. Reno, Opt. Lett. **32,** 2840 (2007).
16. S. Kumar, Q. Hu, and J. L. Reno, Appl. Phys. Lett. **94,** 131105 (2009).
17. S. Kumar, C. W. I. Chan, Q. Hu, and J. L. Reno, Appl. Phys. Lett. **95,** 141110 (2009).
18. B. S. Williams, H. Callebaut, S. Kumar, Q. Hu, and J. L. Reno, Appl. Phys. Lett. **82,** 1015 (2003).
19. G. Scalari, L. Ajili, J. Faist, H. Beere, E. Linfield, D. Ritchie, and G. Davies, Appl. Phys. Lett. **82,** 3165 (2003).
20. R. Köhler, A. Tredicucci, C. Mauro, F. Beltram, H. E. Beere, E. H. Linfield, A. G. Davies, and D. A. Ritchie, Appl. Phys. Lett. **84,** 1266 (2004).
21. G. Scalari, N. Hoyler, M. Giovannini, and J. Faist, Appl. Phys. Lett. **86,** 181101 (2005).
22. S. Kumar and A. W. M. Lee, IEEE J. Sel. Topics Quantum Electron. **14,** 333 (2008).
23. G. Scalari, M. I. Amanti, C. Walther, R. Terazzi, M. Beck, and J. Faist, Opt. Express **18,** 8043 (2010).
24. M. Rochat, L. Ajili, H. Willenberg, J. Faist, H. Beere, G. Davies, E. Linfield, and D. Ritchie, Appl. Phys. Lett. **81,** 1381 (2002).
25. S. Kumar, B. S. Williams, Q. Hu, and J. L. Reno, Appl. Phys. Lett. **88,** 121123 (2006).
26. B. S. Williams, S. Kumar, H. Callebaut, Q. Hu, and J. L. Reno, Appl. Phys. Lett. **83,** 2124 (2003).

27. H. Luo, S. R. Laframboise, Z. R. Wasilewski, G. C. Aers, H. Liu, and J. Cao, Appl. Phys. Lett. **90,** 041112 (2007).
28. S. Kumar, Q. Hu, and J. L. Reno, in *Proceeding of OSA Technical Digest*, CThH4 (2009). Http://www.opticsinfobase.org/abstract.cfm?URI=CLEO-2009-CThH4.
29. H. Callebaut and Q. Hu, J. Appl. Phys. **98,** 104505 (2005).
30. R. Nelander and A. Wacker, Appl. Phys. Lett. **92,** 081102 (2008).
31. M. A. Belkin, J. A. Fan, S. Hormoz, F. Capasso, S. Khanna, M. Lachab, A. G. Davies, and E. H. Linfield, Opt. Express **16,** 3242 (2008).
32. C. Sirtori, F. Capasso, J. Faist, A. L. Hutchinson, D. L. Sivco, and A. Y. Cho, IEEE J. Quantum Electron. **34,** 1722 (1998).
33. S. Kumar and Q. Hu, Phys. Rev. B **80,** 245316 (2009).
34. C. Walther, M. Fischer, G. Scalari, R. Terazzi, N. Hoyler, and J. Faist, Appl. Phys. Lett. **91,** 131122 (2007).
35. C. Walther, G. Scalari, J. Faist, H. Beere, and D. Ritchie, Appl. Phys. Lett. **89,** 231121 (2006).